HAL
open science

West African Squall-Line Thermodynamic Structure Retrieved from Dual-Doppler Radar Observation

Frank Roux, Jacques Testud, Marc Payen, Bernard Pinty

To cite this version:

Frank Roux, Jacques Testud, Marc Payen, Bernard Pinty. West African Squall-Line Thermodynamic Structure Retrieved from Dual-Doppler Radar Observation. Journal of the Atmospheric Sciences, 1984. hal-01974995

HAL Id: hal-01974995

https://uca.hal.science/hal-01974995v1

Submitted on 8 Jun 2021

HAL is a multi-disciplinary open access archive for the deposit and dissemination of scientific research documents, whether they are published or not. The documents may come from teaching and research institutions in France or abroad, or from public or private research centers.

L'archive ouverte pluridisciplinaire **HAL**, est destinée au dépôt et à la diffusion de documents scientifiques de niveau recherche, publiés ou non, émanant des établissements d'enseignement et de recherche français ou étrangers, des laboratoires publics ou privés.

West African Squall-Line Thermodynamic Structure Retrieved from Dual-Doppler Radar Observations

FRANK ROUX AND JACQUES TESTUD

Centre de Recherches en Physique de l'Environnement Terrestre et Planétaire (CNET/CRPE), 92131 Issy-les-Moulineaux, France

MARC PAYEN

Centre National de Recherches Météorologiques, (DMN/EERM), 31057 Toulouse Cedex, France

BERNARD PINTY

Laboratoire Associé de Météorologie Physique, Université de Clermont II, BP 45, 63170 Aubière, France

(Manuscript received 3 August 1983, in final form 17 August 1984)

ABSTRACT

Pressure and temperature fields within a West African squall line, retrieved from dual-Doppler radar data collected during the "COPT 81" (Convection Profonde Tropicale) experiment are presented. The method for derivation of these results is approximately similar to that proposed by Gal-Chen, based on the anelastic equation of motion.

Comparisons between pressure and temperature fields deduced from radar data at the lowest levels and surface network measurements show good agreement. The inferred thermodynamic structure displays the influence of a low-level frontward flow which is mainly due to a density current of cold air, generated in the stratiform region of the squall line and resulting from a mesoscale downdraft. This frontward flow contributes to initiate and maintain a frontal updraft through both nonhydrostatic pressure perturbation and temperature difference between entering air and colder frontward flow. At higher altitudes, mixing with the environment reduces buoyancy in the frontal updraft, while weaker convective updrafts develop in the inner region.

Comparisons between these results and the kinematic and thermodynamic structures deduced from a previous observation (Le Mone, 1983) display different types of dynamics of organized convective systems.

1. Introduction

During the past decade, numerous observational and numerical studies have been devoted to deep convection, leading to more accurate descriptions of air motion and precipitation processes. The improvement of three-dimensional and time-dependent numerical models has been such that they are now able to provide a detailed representation of the kinematic, thermodynamic and moisture (liquid and vapor) fields within a convective flow (e.g., Wilhelmson, 1974; Schlesinger, 1978; Cotton and Tripoli, 1978; Klemp and Wilhelmson, 1978). Concurrently, progress in Doppler radar technique and data analysis has been accomplished and the present capabilities are such that a reliable description of the three-dimensional wind fields within a storm, with a resolution similar to that of numerical models (i.e., $1 \times 1 \times 0.5$ km^3), can be achieved using a properly designed multiple-Doppler radar experiment (e.g., Ray *et al.*, Kropfli and Miller, 1976; Heymsfield, 1978).

A better understanding of the dynamics of deep convection should arise from a closer relationship between both the modeling and experimental approaches. A significant effort in that direction has been presented by Klemp *et al.* (1981) who have studied the detailed structure of a supercell tornadic storm through the interactive use of Doppler radar data and of a three-dimensional numerical simulation. It has also been proposed that the modeling approach be more directly used for interpreting the experimental wind fields. In particular Gal-Chen (1978), Hane and Scott (1978), Hane *et al.* (1981) have considered that these experimental wind fields should obey the equation of motion. They have shown that the associated pressure and temperature perturbation fields could be retrieved from these data. In order to test their method, these authors have used output from numerical models instead of observations and have obtained quite encouraging results.

To our knowledge, the first attempt to apply such a method to real observations was presented by Chong *et al.* (1980). The horizontal gradients of pressure and temperature perturbation, derived from a dual-Doppler radar observation of a moderate storm, displayed, in particular, the generation of

© 1984 American Meteorological Society

Unauthenticated | Downloaded 06/08/21 12:46 PM UTC

pressure gradients through the interaction of vertical motions and horizontal wind shear. Also the counteractive behavior of the vertical pressure gradient and buoyancy forces was shown. However, although these results seemed plausible (similar features have been deduced from observations or numerical models), the validity of the method could not actually be assessed because of the lack of data allowing verifications. Encouraging results have also been obtained in the retrieval of thermodynamic variables from radar data for various meteorological situations (Hane and Gal-Chen, 1982; Pasken and Lin, 1982; Gal-Chen and Kropfli, 1983; Roux *et al.*, 1983).

The present paper is a continuation of this effort. Here the experimental wind fields are obtained from dual-Doppler radar observation of a continental West-African squall line, performed during the "COPT 81" (Convection Profonde Tropicale) experiment. This case study seems particularly appropriate to check the validity of the pressure and temperature fields retrieved from actual observations; first, because of the existence of simultaneous measurements of pressure and temperature at ground level, and then, because of the quite simple structure of the observed squall line which facilitates the interpretation and the comparison with the verification data.

Section 2 recalls the principles of the analysis and describes, in details, the variational method used to retrieve pressure and temperature fields. In section 3, after a brief description of the observed squall line, the thermodynamic fields deduced are compared with surface network data; the inferred thermodynamic structure of the squall line is discussed and compared with previous similar observations.

2. The retrieval of pressure and temperature perturbations from radar data

a. Principles of the analysis

We assume, through an elaborate processing of the radial velocity fields observed in a multiple-Doppler radar experiment, that we have obtained a reliable representation of the three-dimensional air motion field within the precipitating region of a storm. Through an approach similar to that developed by Gal-Chen (1978), we consider the first order "anelastic" approximation of the equation of motion. Following Wilhelmson (1974), it may be written as

$$\frac{D\mathbf{V}}{Dt} = \underbrace{\frac{\partial \mathbf{V}}{\partial t} + (\mathbf{V}\cdot\nabla)\mathbf{V}}_{\text{(a)}} = \underbrace{-C_p\theta_{V0}\nabla\pi_1}_{\text{(b)}} + \underbrace{g\left[\frac{\theta_{V1}}{\theta_{V0}} - q_l\right]\mathbf{k}}_{\text{(c)}} + \underbrace{\mathbf{S}}_{\text{(d)}}, \quad (1)$$

where $\mathbf{V}$ is the air velocity; ∇ the three-dimensional del operator; C_p the specific heat of moist air at constant pressure; θ_V is the virtual potential temperature defined as $\theta_V = (1 + 0.61q_V)\theta$ where θ is the potential temperature and q_V the mixing ratio of water vapor; π is the nondimensional pressure defined as $\pi = (P/1000 \text{ mb})^K$ where P is the dimensional pressure expressed in hPa (or mb) and $K = (C_p - C_v)/C_v$ where C_v is the specific heat of moist air at constant volume; q_l is the mixing ratio of liquid water (including cloud water content q_c and precipitation water content q_r); $g\mathbf{k}$ the vertical acceleration due to gravity; $\mathbf{S}$ denotes the subgrid scale "turbulent" force. Subscript "0" refers to a basic hydrostatic state (deduced from a radiosounding), and subscript "1" to first order perturbations.

Neglecting the Coriolis force, (1) states that the acceleration (a) of an air parcel is equal to the sum of three forces: the pressure force (b), the buoyancy force (c) and the subgrid scale force (d) (forces per unit mass are referred to as forces). The air parcel acceleration is deduced from the components of velocity and their first-order derivatives. The subgrid scale force S may be estimated from the three-dimensional (3D) wind field using a parameterization scheme (here we have used that of Deardorff, 1975; see Gal-Chen, 1978) and the precipitation water contribution q_r to the liquid water content q_l may be deduced from the radar reflectivity values through either an empirical or experimental relation. Then, to isolate in (1) the respective contributions of pressure and temperature perturbations the following procedure is used:

i) Horizontally (1) reduces to

$$\nabla_H(\pi_1) = \mathbf{A}_H \quad (2)$$

with

$$\mathbf{A}_H = \frac{-(D\mathbf{V}_H/Dt - \mathbf{S}_H)}{C_p\theta_{V0}},$$

where subscript H denotes two-dimensional horizontal vectors. (2) implies that the horizontal gradients may be derived from the experimental estimates of $\mathbf{A}_H$, and then pressure perturbations π_1 may be deduced, except for a constant, depending only on altitude. Difficulty in solving (2) arises from errors in the experimental data and possible inadequacies in parameterizations. Thus $\mathbf{A}_H$ is not formally identical to a horizontal gradient.

ii) Vertically, (1) is written as

$$\frac{Dw}{Dt} = -C_p\theta_{V0}\frac{\partial\pi_1}{\partial z} + g\left[\frac{\theta_{V1}}{\theta_{V0}} - q_l\right] + S_z. \quad (3)$$

Then, to deduce temperature perturbations the respective contributions of vertical pressure gradient and buoyancy have to be separated. Taking the

Unauthenticated | Downloaded 06/08/21 12:46 PM UTC

horizontal derivative of (3) and considering the derivatives of π_1 in a reverse order, we obtain

$$\nabla_H\left[\frac{Dw}{Dt}\right] = -C_p\theta_{V0}\frac{\partial}{\partial z}[\nabla_H\pi_1] + g\nabla_H\left[\frac{\nabla_{V1}}{\theta_{V0}} - q_l\right] + \nabla_H S_z.$$

Using (2), an equation for the temperature perturbation, similar to that for the pressure, may be derived, i.e.:

$$\nabla_H(\theta_{C1}) = \mathbf{B}_H \tag{4}$$

with

$$\mathbf{B}_H = \frac{C_p\theta_{V0}^2}{g}\left[\frac{\partial}{\partial z}(\nabla_H\pi_1)\right] + \theta_{V0}\nabla_H\left[\frac{Dw}{Dt} + gq_r - S_z\right],$$

where $[Dw/Dt, S_z$ and $q_r]$ are calculated from radar data, and π_1 is the pressure field determined from (2). In (4) we introduce a "virtual cloud temperature" perturbation θ_{C1} which takes into account both virtual temperature perturbation θ_{V1} and cloud water content q_c as

$$\theta_{C1} = \theta_{V1} - q_c\theta_{V0}. \tag{5}$$

Since (4) is similar to (2), the experimental $\mathbf{B}_H$ is not formally identical to the horizontal gradient $\nabla_H(\theta_{C1})$ and "cloud temperature" perturbation cannot be directly calculated.

b. *The method used for calculating the pressure and temperature perturbation fields*

To verify (2), $\mathbf{A}_H$ should be curl-free ($\nabla_H \times \mathbf{A}_H = 0$) but unavoidable errors in the experimental estimates of $\mathbf{A}_H$ (radar statistical error, differentiation scheme, parameterization of subgrid processes . . .) make the direct integration of (2) impossible. The present approach consists in determining at each altitude z_0 a function $\pi_1(x, y, z_0)$, solution of the variational problem formulated as follows:

i) the horizontal gradient of $\pi_1(x, y, z_0)$ should be "close", in the least squares sense, to the data field $\mathbf{A}_H$;

ii) the contribution of error in the obtained pressure field $\pi_1(x, y, z_0)$ should be filtered as far as possible.

More specifically, this may be expressed as the minimization of a functional F written as:

$$F = \iint_{D(z_0)} [\nabla_H\pi_1 - \mathbf{A}_H]^2 dxdy + \mu \iint_{D(z_0)} [C(\pi_1)]dxdy \tag{6}$$

with

$$C(\pi_1) = \left[\frac{\partial^2\pi_1}{\partial x^2}\right]^2 + \left[\frac{\partial^2\pi_1}{\partial y^2}\right]^2 + 2\left[\frac{\partial^2\pi_1}{\partial x\partial y}\right]^2,$$

where $D(z_0)$ denotes the horizontal domain at altitude z_0, where data $\mathbf{A}_H$ are available.

In (6) functional F_1 forces the retrieved pressure gradient to be close to the data field $\mathbf{A}_H(x, y, z_0)$, and F_2 is a constraint (with a weight μ) introduced to filter out small scale variations of π_1. By considering the Euler equation associated to (6) and rewriting it in the Fourier space, it may be shown that constraint F_2 acts as a *low-pass* filter which has the property of isotropy and whose amplitude gain has the form

$$G(k) = [1 + (k/k_0)^2]^{-1},$$

where the cutoff wavenumber k_0 is controlled by the value of the weight μ as

$$k_0 = \mu^{-1/2}.$$

In practice μ is chosen equal to $0.35\Delta^2$ (where Δ is the horizontal grid spacing) where the corresponding cutoff wavelength (3.7Δ) is that of the analysis of the raw Doppler velocity data used to obtain the 3D wind field. Constraint F_2 avoids the introduction of a spurious signal (numerical noise) in the spectral band $[\lambda < 3.7\Delta]$ which cannot be exploited as a physical signal from the 3D wind field. It is to be noted that, even in absence of term F_2, the minimization of (6) tends to filter out the experimental error. If ϵ_H is the vector error in $\mathbf{A}_H$, it may be dissociated in two parts, one being curl-free in the horizontal plane, and the other being divergence-free. It is obvious that the divergence-free part of ϵ_H will be eliminated through the minimization of F_1.

A classical approach to solve (6) for π_1 is to consider the associated Euler equation and to integrate it with "natural" boundary conditions (Courant and Hilbert, 1953). Here, we prefer the approach proposed by Wahba and Wendelberger (1980) and also used by Testud and Chong (1983), starting from direct discretization of F through a finite difference approximation. The values $\pi_1(x, y, z_0)$ are obtained by inversion of a matrix whose dimensions are $N \times N$, where N is the total number of points in the horizontal grid domain. The advantage of this procedure is that the truncation at the edges of the domain automatically generates the boundary conditions needed for integration. It is to be emphasized that, through this procedure, difficulties in integrating the Euler equation in presence of irregular boundaries or missing data cancel out. These points are given in detail in Appendix A.

For convenience, the results are expressed in terms of dimensional pressure perturbations P_1 (in hPa or mb), related to the nondimensional pressure perturbations π_1 through:

$$P_1 = [C_p\theta_{V0}\rho_0]\pi_1,$$

where θ_{V0} and ρ_0 are the virtual potential temperature and density in the unperturbated state at the altitude

Unauthenticated | Downloaded 06/08/21 12:46 PM UTC

considered. This method also applies to the determination of the "virtual cloud temperature" $\theta_{C1}(x, y, z_0)$ perturbations, as solution of (4) for each altitude.

3. Application to the observation of a West African squall-line

a. The squall-line observed on 22 June 1981

The present data refer to the observation of a continental West African squall line during the "COPT 81" (Convection Profonde Tropicale) experiment carried out at Korhogo in the North of Ivory Coast, during May and June 1981 by French and Ivorian research institutes. A complete description of the different measurements conducted, of the scientific aims, and an overview of some preliminary results may be found in Sommeria and Testud (1984).

The event in question has been observed with help of the RONSARD dual-Doppler radar system of the "Centre de Recherches en Physique de l'Environnement" (C.R.P.E.) on 22 June 1981 from 0200 till 1000 (all times are local times: GMT). As the radar observations were taken, simultaneous measurements from a surface network were performed (Fig. 1). Two kinds of automatic stations were operated

i) the DELTA stations from the "Etablissement d'Etudes et de Recherches Météorologiques" in the western part of the scanning area;

ii) the ALICE I and ALICE II stations from the "Laboratoire Associé de Météorologie Physique" in the eastern part.

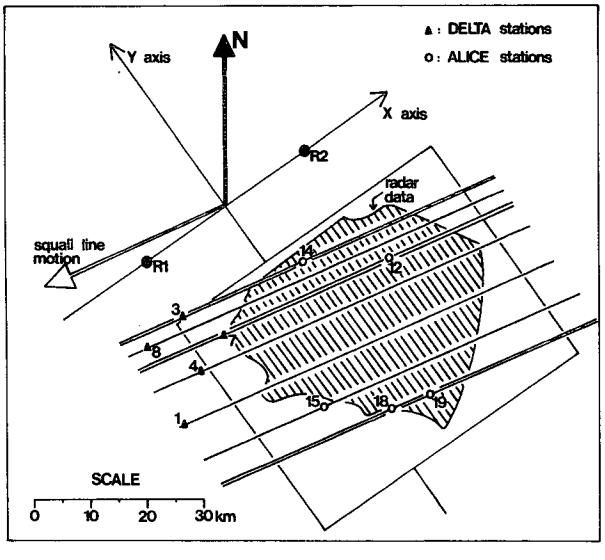

FIG. 1. Location and equivalent trajectories (see text) of DELTA and ALICE surface stations with respect to the radar data domain. Location of the RONSARD radars, squall-line motion, north direction and X and Y axes are indicated.

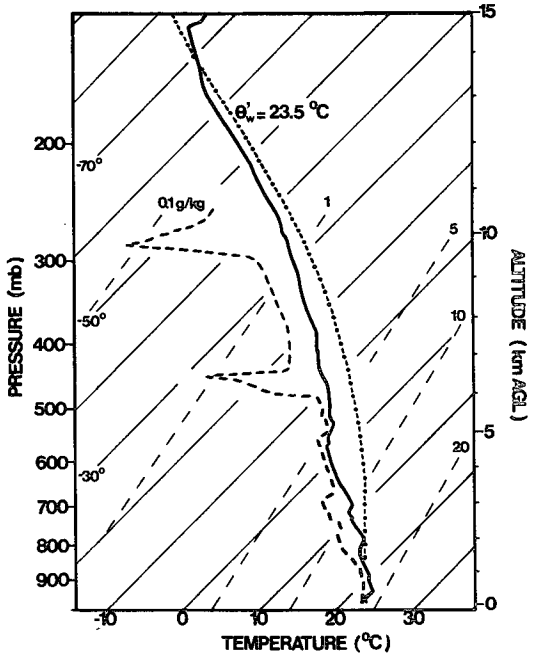

FIG. 2. Skew T–log$P$ diagram indicating vertical thermodynamic structure of the atmosphere at Korhogo on 22 June 1981 at 0348 GMT. A moist adiabat (θ'_w = 23.5°C) represents the ascent of an undiluted parcel.

These stations allowed a detailed automatic recording of the main meteorological variables (every 2 min 30 s for the DELTA and every 30 s for the ALICE): temperature, humidity, wind direction and intensity, pressure and rainfall rate (in addition, vertical fluxes measurements were performed with the ALICE I stations). On 22 June 1981, 5 DELTA and 5 ALICE II stations were operational.

The radiosounding, launched at Korhogo 30 min before the arrival of the squall line above the experimental site, reveals a rather moderate instability of the atmosphere upstream (Fig. 2). The bottom layer from ground level to altitude 1200 m (all altitudes are AGL, the mean ground level over the experimental area is 400 m) is potentially unstable. The condensation level for an air parcel lifted from 500 m is 800 m; once lifted to its level of free convection (i.e.: 1200 m) this air parcel would be accelerated, in absence of mixing with the environment, up to the altitude of 13 000 m. The maximum buoyancy would be obtained around 4500 m with a 5°C potential temperature excess with respect to the environment (which is a quite moderate value when compared to the other observations of squall lines during "COPT 81"). It is worth noting that, although the level of free convection is 1200 m, the buoyancy of the air parcel remains smaller than 1°C up to 2000 m. Moreover, if we take account of the cloud water loading applied to the air parcel, we may calculate that, as long as the precipitation process is not

Unauthenticated | Downloaded 06/08/21 12:46 PM UTC

triggered, the actual buoyancy of the air parcel—temperature buoyancy minus cloud water loading—should remain close to zero up to 2800 m (at this height, the adiabatic water content of the air parcel, i.e. 6.5 g kg^{-1}, equilibrates its temperature excess, i.e. 2°C). It is important to keep in mind this point to understand the dynamics of the squall line presently analyzed.

The mesoscale reflectivity contours (Fig. 3) deduced from a PPI scan at 0453 display features similar to tropical squall lines observed during "GATE" (e.g.: Houze and Betts, 1981):

i) the structures are stationary during the squall line translation (19 m s^{-1} towards southwest);

ii) the maximum reflectivity values (here up to 55 dBZ) are found in the frontal part of the squall-line, hereafter referred to as the "convective region";

iii) lower and more uniform reflectivity values (30 dBZ) are observed in the extended rear part: hereafter referred to as the "stratiform region".

When the convective region arrived above the experimental site, the Doppler radars were operated following the COPLANE methodology (Lhermitte, 1970). 5 COPLANE scans were conducted (at 0357, 0405, 0411, 0418 and 0424) and the three-dimensional wind and reflectivity fields have been obtained through an original processing method whose main characteristics are (for more details see: Testud and Chong, 1983; Chong *et al.*, 1983; Chong and Testud, 1983):

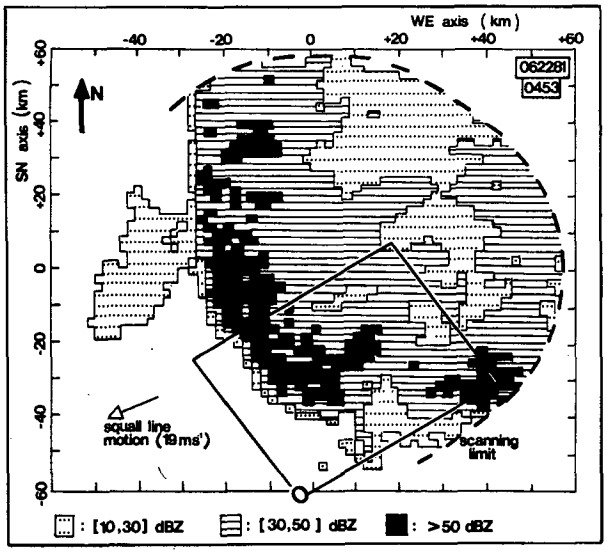

FIG. 3. Reflectivity contours within the altitude range (0.5, 1.5 km AGL) deduced from the 0453 PPI scanning. The solid line contour displays the area where the 3D wind fields have been obtained from the COPLAN scannings (X and Y axes and origin of the coordinates are indicated). Squall-line motion and north direction are also indicated.

i) advection (i.e.: cloud displacement during data acquisition) is taken into account using a mathematically exact formalism;

ii) error in the vertical component of velocity is minimized through the use of a variational concept to determine the boundary condition for integrating the continuity equation;

iii) stability of the wind field with respect to first order differentiation is insured through a filtering technique similar to that described in section 2b.

Our aim is not here to give a complete description of the air flow associated to the squall-line; such a description may be found in Roux *et al.* (1982) and Chong (1983). In this paper, which is focused on the dynamics of the convective region, we will restrict to recall the main characteristics of the three-dimensional wind field in the convective region. These are (Fig. 4):

i) the wind field appears *stationary* in the reference frame moving with the squall line, since very similar results are obtained from the 5 scans (Chong *et al.*, 1983);

ii) the air circulation within the northwestern part of the COPLANE scanning area ($20 < y < 40$ km in Fig. 4a and 4b) is almost *two-dimensional;* i.e. depends mainly on vertical and on horizontal coordinate parallel to the squall line displacement. A representative vertical cross section in this northwestern part is given in Fig. 4c; all the sections for [$20 < y < 40$ km] look like Fig. 4c;

iii) two distinct horizontal flows are observed—a westerly flow entering the squall line at all altitudes due to its displacement at a speed larger than environmental winds, and a low-level easterly flow coming from the rear of the scanning region;

iv) the largest upward velocities are observed in the northwestern region within a frontal updraft ($5 < x < 10$ km in Fig. 4c), with a maximum intensity at altitude 2500 m. Less intense updrafts exist at higher altitude in the inner convective region ($15 < x < 20$ km and $25 < x < 30$ km in Fig. 4c);

v) downward motions (convective downdrafts) are of small extent and weak intensity. These downdrafts do not seem to play an important role in the dynamics of the convective region.

Considering the previous analysis of the radiosounding data, it seems unprobable that the frontal updraft (whose intensity peaks at altitude 2500 m) be driven by buoyancy. One should consider the possibility that the frontal updraft be forced (at least below 2500 m) by the low-level easterly flow through a mechanism analogous to the propagation of a density current (the easterly flow representing here a cold air pool). The retrieval of pressure and temperature fields within the convective region may help us to verify such an interpretation.

Unauthenticated | Downloaded 06/08/21 12:46 PM UTC

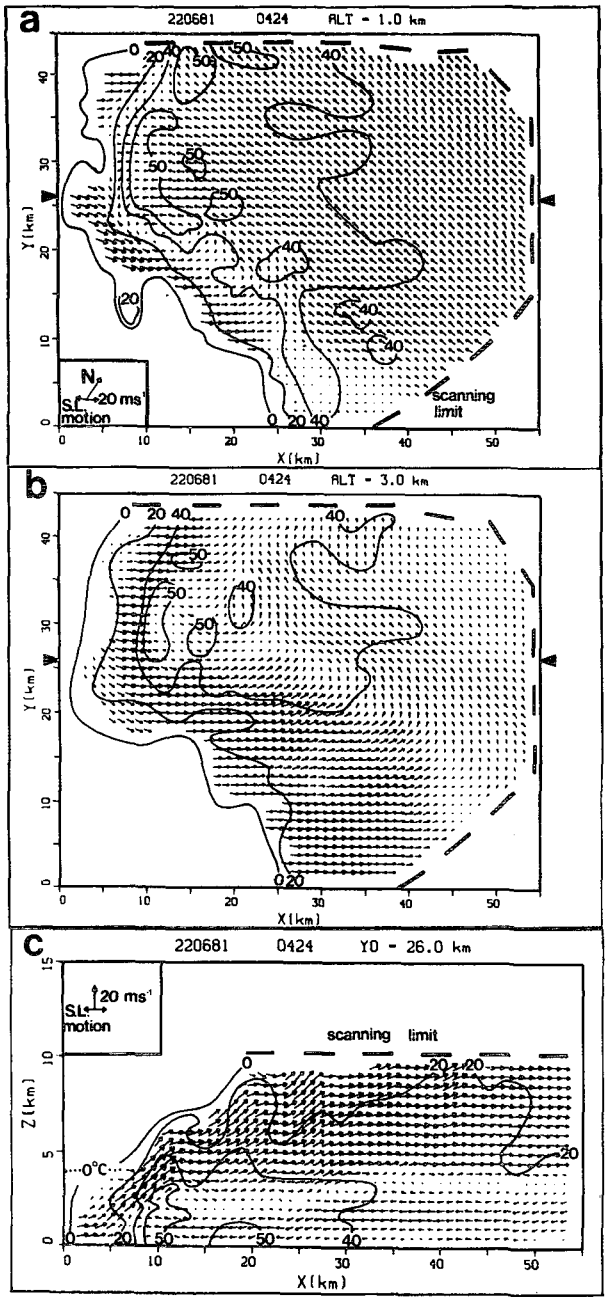

FIG. 4. Horizontal motions (in the frame moving with the squall line) and reflectivity contours (in dBZ) at altitudes 1.0 km (a) and 3.0 km (b) AGL and vertical cross section at y = 26 km (c), deduced from the 0424 sequence. Squall-line motion and the North are indicated.

b. Reliability of the retrieved pressure and temperature fields

We consider here the results deduced from the radar data obtained at 0418 and 0424, so the results will be representative of the intermediate time 0421. As the precipitation front of the squall line entered the COPLAN scanning area at about 0355, wind and reflectivity fields processed from the data obtained at 0357, 0405 and 0411 display incomplete views of the frontal part of the squall line.

Table 1 shows, as functions of altitude and for each cartesian coordinate, the rms values of the different terms in the equation of motion (as deduced from radar data):

i) the temporal evolution $[\partial \mathbf{V}/\partial t]$ estimated through a finite difference scheme between the two successive COPLAN scans;

ii) the advective term $[(\mathbf{V}\cdot\nabla)\mathbf{V}]$;

iii) the subgrid scale force [S] calculated as in Gal-Chen (1978);

iv) the precipitation water loading $[gq_r\mathbf{k}]$, where q_r is estimated from the reflectivity values through a relation deduced from spectropluviometer data ($q_r = 0.173 \times 10^{-2}\, Z^{0.613}$, where q_r is in g m^{-3} and Z in mm^6 m^{-3}).

The main contribution results from the advective term $[(\mathbf{V}\cdot\nabla)\mathbf{V}]$ and the temporal evolution term $[\partial \mathbf{V}/\partial t]$ is relatively weak. Since this last term is deduced from differences between successive scans (with Δt = 350 s), one can only estimate a mean "trend" and the rapid variations of wind cannot be taken into account. Nevertheless, stationarity of the 3D wind and reflectivity fields deduced from the 5 successive scans suggests that temporal evolution should be rather slow so that the approximation used here is likely to be adequate (Chong and Testud, 1983, have shown that the characteristic variation time was 28.6 min, about 5 times larger than the time interval used here).

The subgrid scale force [S] appears to be a weak influence, but as there are various possibilities for estimating this term, different parameterizations could lead to different estimates. Here we have used Deardorff's formulation, as Gal-Chen (1978), and the subgrid eddy viscosity coefficient Km has been determined both from the variance of the Doppler spectra and from the fluctuation of the raw radial velocities with respect to the "filtered" representations (Testud and Chong, 1983). Then, the estimated value of Km is 180 m^2 s^{-1} and the rms value of the standard deviation from the "filtered" velocities is 1.5 m s^{-1}. We have verified that the rms value of Km calculated with Smagorinsky's formulation (Smagorinsky, 1963) is equal to 180 m^2 s^{-1}, when the arbitrary constant C is chosen equal to 0.2, which corresponds to an unstable atmosphere. Moreover, the observed "smoothness" of the 3D wind field (except at the interface between the two opposite flows) indicates that subgrid scale processes should not be of crucial importance here. The contribution of the precipitation water loading $[gq_r]$ is appreciable at low levels.

There are two ways for testing the reliability of the retrieved pressure and temperature perturbation fields.

Unauthenticated | Downloaded 06/08/21 12:46 PM UTC

TABLE 1. Root-mean-square values of the three components of the different terms in the equation of motion for successive altitudes, in 10^{-2} m s^{-2} (the subgrid scale for **S** cannot be calculated at the lowest level 0.75 km as it includes second order derivatives).

Altitude (km)	$\partial U/\partial t$	$(\mathbf{V}\cdot\nabla)u$	S_x	$\frac{\partial V}{\partial t}$	$(\mathbf{V}\cdot\nabla)v$	S_y	$\frac{\partial W}{\partial t}$	$(\mathbf{V}\cdot\nabla)w$	S_z	gq_r
0.75	0.8	1.4		0.4	0.8		0.4	0.9		1.0
1.75	0.9	2.9	0.5	0.3	1.2	0.2	0.5	1.6	0.2	1.0
2.75	1.0	3.0	0.5	0.4	1.3	0.2	0.6	2.1	0.3	0.8
3.75	1.1	2.6	0.3	0.5	1.5	0.1	0.6	2.5	0.2	0.6
4.75	0.8	1.9	0.2	0.6	1.8	0.1	0.6	2.6	0.1	0.3

First, one may estimate mathematically the influence of *statistical* error in both input and output data; however, *systematic* errors (bias) may escape notice in such calculation. Then, a complementary possibility is a comparison between the radar-derived results and independent measurements of the same parameters.

A priori and *a posteriori* estimates of statistical uncertainty (see Appendix B) in both input data $\mathbf{A}_H$ in (2) and $\mathbf{B}_H$ in (4) and retrieved results $[\nabla_H P_1]$ and $[\nabla_H \theta_{C1}]$ are listed for different altitudes in Tables 2 and 3. The "momentum-checking" parameter E_R, defined by Gal-Chen and Hane (1981) as (e.g. for pressure):

$$E_R = \frac{\iint_{D(z_0)} [\nabla_H \pi_1 - \mathbf{A}_H]^2 dxdy}{\iint_{D(z_0)} \mathbf{A}_H{}^2 dxdy}$$

is also listed; E_R is a measure of how the retrieved pressure and temperature fields fit the experimental estimates $\mathbf{A}_H$ and $\mathbf{B}_H$. As deduced from numerical experiments with simulated data (see Appendix B), if $\mathbf{A}_H$ or $\mathbf{B}_H$ are error-free, E_R is less than 0.10 (depending on the characteristic wavelength) but it is not equal to zero because of finite difference approximations. On the other hand, if $\mathbf{A}_H$ or $\mathbf{B}_H$ are both random (white) noise, E_R is equal to a maximum value of 0.60. It is to be noted that, because of the filtering of small scale phenomena due to constraint (F_2) in (6), this maximum value of E_R is larger than that (0.50) found by Gal-Chen and Hane (1981). As seen in Tables 2 and 3, as the present values of E_R are always within the interval [0.14, 0.45], the retrieved thermodynamic fields should be realistic to some degree. Moreover the fair correlation between *a priori* and *a posteriori* estimates indicates that statistical errors due to the approximations used for calculating temporal evolution, subgrid scale force and precipitation water content are probably smaller than the radar statistical error. The estimated *statistical* uncertainties in the retrieved pressure and temperature gradients are less than 0.1 mb km^{-1} and 0.5°C km^{-1}.

Accuracy of the radar-derived results has also been tested through comparisons with surface measurements of pressure and temperature. In this way the presence of hypothetical *systematic* errors, which could escape notice in the estimates of *statistical* error, should be revealed. Assuming stationarity in the frame moving with the squall line (as suggested by radar observations) temporal measurements from each surface station may be transformed into spatial measurements along axes crossing the stations and parallel to the squall line motion (Fig. 1). Then, referring to the time of radar observation (0421), these spatial measurements may be directly compared with those depicted from the analysis of radar data. However, as radar data are not available at ground level, the values measured at ground with the ALICE and DELTA stations will be compared to the results obtained from radar data at the lowest levels (i.e., 750 m AGL for pressure and 1000 m AGL for temperature). As mentioned in Section 2, the radar-derived pressure and temperature fields deviate from the true values by an arbitrary constant, since the analysis provides pressure and temperature fields whose mean value within the horizontal domain is arbitrarily taken to be null. Therefore, a constant is added to the radar-derived results in order to compensate this effect; the constant is determined as that leading to the best fit with surface measurements, and is +0.6 mb for pressure and −4°C for temperature.

These comparisons, displayed in Fig. 5 for pressure and in Fig. 6 for temperature, show a satisfying agreement between the two kinds of results. The pressure decrease follows very similar slopes and, as

TABLE 2. The *a priori* σ_s and *a posteriori* σ_e estimates of statistical uncertainty in the input data $\mathbf{A}_H$, rms values of $\mathbf{A}_H$, "momentum-checking" parameter E_R and estimated statistical uncertainty in the retrieved pressure gradients $\sigma_e(\nabla_H P_1)$, for successive altitudes. All quantities (except E_R) are expressed in hPa km^{-1}.

Altitude (km)	$\sigma_s(\mathbf{A}_H)$	$\langle \mathbf{A}_H{}^2 \rangle^{1/2}$	E_R	$\sigma_e(\mathbf{A}_H)$	$\sigma_e(\nabla_H P_1)$
0.75	0.14	0.18	0.29	0.12	0.05
1.75	0.13	0.24	0.14	0.11	0.05
2.75	0.14	0.25	0.26	0.16	0.07
3.75	0.14	0.21	0.41	0.17	0.08
4.75	0.12	0.17	0.40	0.14	0.06

Unauthenticated | Downloaded 06/08/21 12:46 PM UTC

TABLE 3. The *a prior* σ_s and *a posteriori* σ_e estimates of statistical uncertainty in the input data $\mathbf{B}_H$, rms value of $\mathbf{B}_H$, "momentum-checking" parameter E_R and estimated statistical uncertainty in the retrieved "cloud" temperature gradients $\sigma_e(\nabla_H\theta_{C1})$, for successive altitudes. All quantities (except E_R) are expressed in °C km^{-1}.

Altitude (km)	$\sigma_s(\mathbf{B}_H)$	$\langle \mathbf{B}_H^2 \rangle^{1/2}$	E_R	$\sigma_e(\mathbf{B}_H)$	$\sigma_e(\nabla_H\theta_{C1})$
1.0	0.40	0.60	0.36	0.45	0.20
2.0	0.50	0.95	0.27	0.65	0.30
3.0	0.60	0.85	0.35	0.65	0.30
4.0	0.85	1.10	0.36	0.85	0.35
5.0	1.00	1.30	0.43	1.10	0.50

seen when comparing with ALICE 12 and DELTA 1, 4, 7, amplitude and location of the peak deduced from radar data corroborate the surface measurements. With regard to temperature, the well defined drop is found at the same place with a similar amplitude (ALICE 12 and DELTA 1, 4, 7) and after this transition relatively flat profiles are jointly observed.

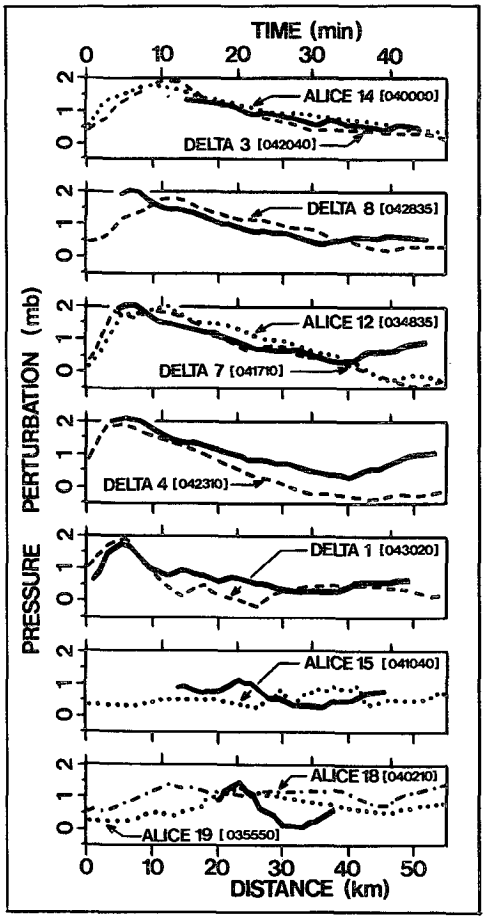

FIG. 5. Pressure profiles measured with the DELTA (dashed lines) and ALICE (dotted lines) stations, and deduced from radar data (solid lines). The origin of the time axis is indicated for each station.

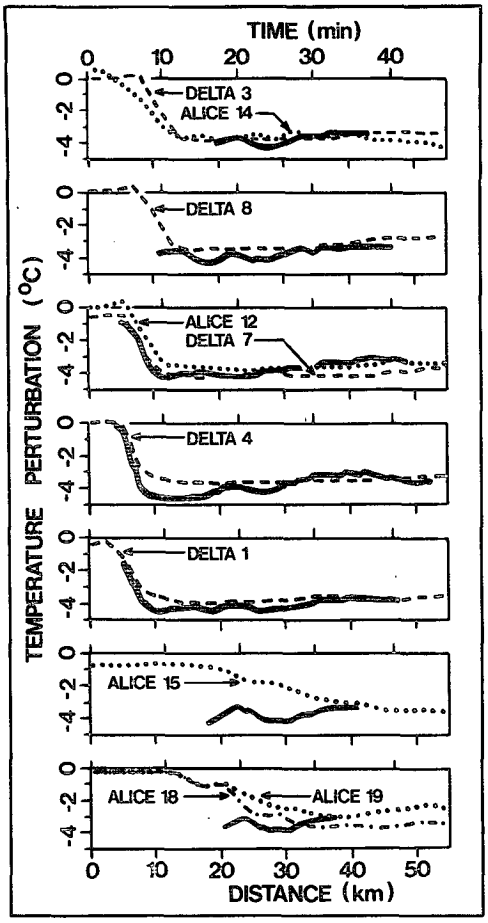

FIG. 6. As in Fig. 4 but for temperature.

It should be noted that, at the low altitudes considered here, the cloud water content q_c (included in the radar-derived "virtual cloud" temperature perturbation θ_{C1}) should not be very large (since the condensation level is at 800 m), so that the "virtual cloud" temperature coincides with the real temperature measured by the stations.

In the southeastern region (ALICE 15, 18 and 19) the observed differences between the radar-derived results and the surface measurements results probably from temporal evolution in both pressure and temperature. This appears when comparing data from ALICE 18 and 19 (time lag for measuring the same region is 6 min 30 s), whereas data recorded in the northwestern part of the scanning area with DELTA 3 and ALICE 14 (time lag: 20 min 40 s) and with DELTA 7 and ALICE 12 (time lag: 28 min 40 s) appear very similar. Since the validity of the comparison between surface data and radar-derived results is subject to the assumption of stationarity, it is not surprising to obtain less agreement in this southeastern region.

Unauthenticated | Downloaded 06/08/21 12:46 PM UTC

c. *Retrieved thermodynamic structure*

The method gives access to the "virtual cloud temperature" θ_{C1} defined in (5) (i.e. virtual temperature corrected for cloud water loading). For simplification, the word "temperature" is used in the following, to denote θ_{C1}; the actual meaning of this "temperature" should not be forgotten.

Pressure and temperature fields retrieved at successive altitudes are shown in Fig. 7 to 11. As mentioned before, these results represent relative values, i.e., fluctuations with respect to a horizontal mean value. Therefore, although information may be deduced from the results retrieved at the same altitude, neither vertical variations nor perturbations with respect to the precipitation-free environment can be inferred. Consequently vertical cross sections of pressure or temperature cannot be drawn from the results obtained at the successive altitudes.

At the lowest levels (750 m for pressure and 1 km for temperature), the main features observed on the retrieved pressure and temperature fields (Fig. 7a and 7b) are the following:

i) a maximum pressure perturbation (up to 1.5 mb with respect to the mean) at the interface between the two opposite flows;

ii) a 4°C temperature drop between the entering flow and the frontward flow.

Previous observations of thunderstorms or squall-line gust fronts have displayed similar results. Following Charba (1974) the weather changes that typify the arrival of a gust front at ground are: a rise in the surface pressure followed by a quick change in wind direction and a rapid temperature drop; the peak wind gust and maximum rain intensity successively follow the "temperature break". On a larger scale, Johnson and Nicholls (1983) found that the passage of a squall line on 12 September 1974 during "GATE" was accompanied at ground by a pressure mesohigh at 1.4 mb and a sudden drop in temperature of about 4°C. Following the analysis of Wakimoto (1982) for thunderstorm gust fronts, the pressure field observed at ground level with the surface stations (Fig. 5) and at low-level (Fig. 7a) from the radar data may be explained through both hydrostatic and nonhydrostatic effects:

i) a hydrostatic pressure difference between the entering flow and the inner convective region results from the different vertical structures of the air above. From the radiosounding data obtained before (0348) and after (0849) it may be found that this hydrostatic pressure difference, is relatively small (about 0.5 mb larger in the inner region than in the entering flow);

ii) a nonhydrostatic pressure rise at the interface between the two flows is due to the collision between warm entering air and cold low-level flow. Its amplitude with respect to the hydrostatic pressure in each air mass, is given by

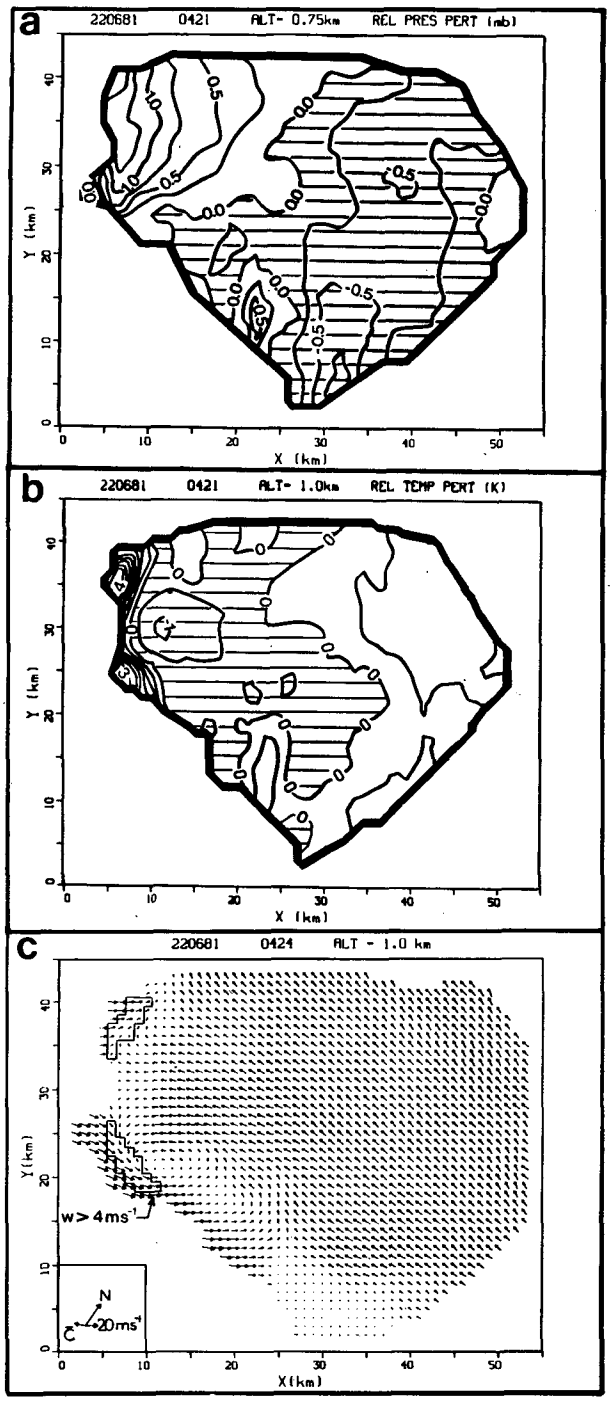

FIG. 7. Relative pressure (a) and temperature (b) perturbation fields and horizontal wind field (c) at altitudes 0.75 km (pressure) and 10 km (temperature and wind field). Steps in the contours are, respectively, 0.25 mb and 0.5 K; hatched zones denote negative values. Updraft regions (vertical velocity larger than 4 m s^{-1}) are indicated in (c).

Unauthenticated | Downloaded 06/08/21 12:46 PM UTC

$$\Delta P_{1,2} = \frac{1}{2}\rho_{1,2}\mathbf{v}_{1,2}^2,$$

where ρ and $\mathbf{v}$ are respectively the air density and air velocity (with respect to the pseudo cold front), in the warm flow (subscript 1) and in the cold flow (subscript 2).

From the observed velocities, and assuming a temperature drop of 4°C between the two flows, it may be calculated that the pressure bump at the pseudo-cold front should be 1.6 mb (ΔP_1) with respect to the warm flow, and 1.1 mb (ΔP_2) with respect to the cold flow, in agreement with the pressure observation at ground (Fig. 5). So the nonhydrostatic pressure perturbation seems the dominant effect at ground level.

At 1750–2000 m (Fig. 8), the pressure and temperature perturbation fields have basically the same morphology as at 750–1000 m, and the same interpretation applies. At 2750–3000 m (Fig. 9), the gross features appears similar as below. Nevertheless a careful examination reveals that

i) the pressure high is shifted upstream, and is observed *ahead the updraft* (Fig. 9a);

ii) the signature of the temperature perturbation does not appear any more as a mere temperature drop from West to East (as at the altitudes below). A zone of *maximum temperature* (+3°C with respect to the mean) may be clearly identified and it *coincides with the zone of frontal updraft* (Fig. 9b).

These two features should be interpreted in a somewhat different way from below: First, the pressure high at 2250 m should result from an obstacle effect of the frontal updraft for the unperturbed environmental inflow. Second, the temperature maximum in the updraft indicates a positive buoyancy with respect to the unperturbed environment at the same height. Thus, below about 2500 m, the updraft seemed to be forced by the frontal propagation of a cold air pool from rear, while at 3000 m it becomes to be driven by thermal buoyancy.

In the southeastern region ($0 < y < 20$ km), a secondary maximum appears at $X = 22$ km in association with another updraft, and between the two pressure high ($10 < x < 20$ km) air entering the squall line is entrained in the low-level frontward flow. As it can be seen in Fig. 3 a discontinuity in the high reflectivity (greater than 50 dBZ) frontal region is observed at this location. Moreover, as deduced from the ALICE 18 and 19 measurements, the dynamic fields appear less stationary than in the northwestern region. Therefore, the dynamic in the southeastern region is certainly more complex than in the northwestern one, where the kinematic, thermodynamic and precipitation structures are almost two-dimensional and stationary.

From 3750 m and above (Figs. 10 and 11), the retrieved thermodynamic structure changes. Pressure perturbations are weaker (less than ±0.75 mb with respect to the mean) and result probably from hydrostatic effects. As a matter of fact, in the inflow region the warm air layer below 2000 m is capped by colder air (Fig. 2), while in the inner region, the cold low level flow is capped by warmer air from the frontal

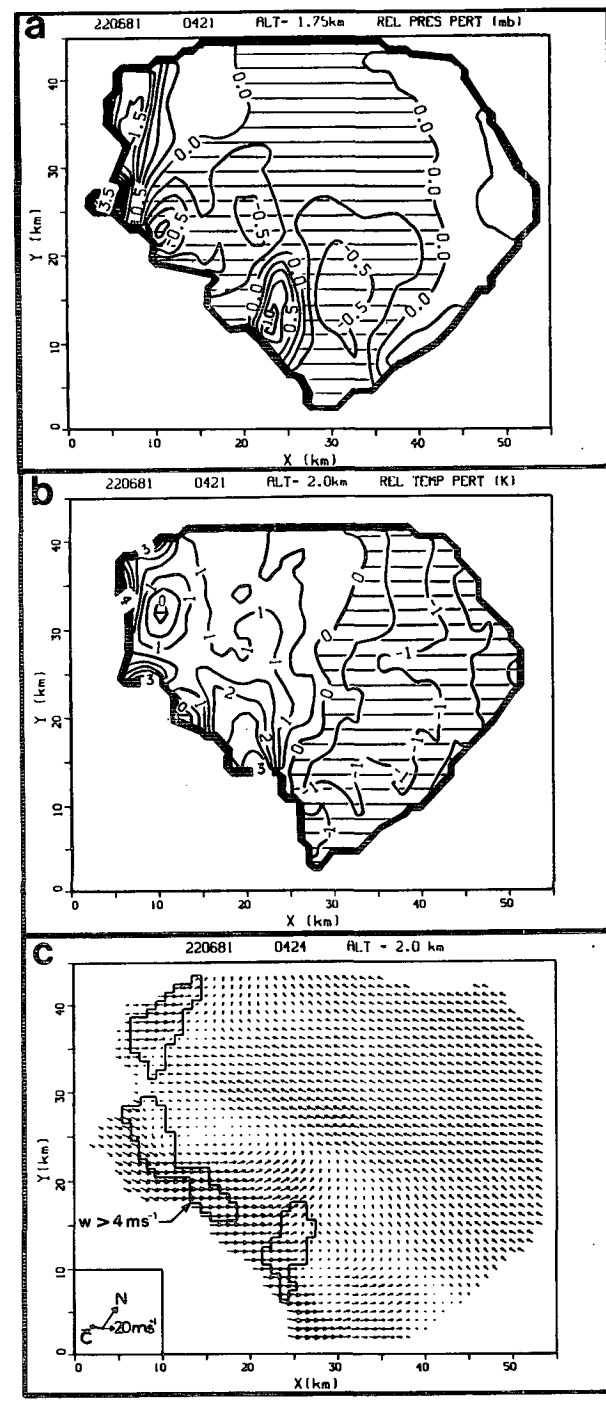

FIG. 8. As in Fig. 7 but for altitudes 1.75 km [pressure in (a)] and 2.0 km [temperature in (b) and horizontal wind field in (c)].

Unauthenticated | Downloaded 06/08/21 12:46 PM UTC

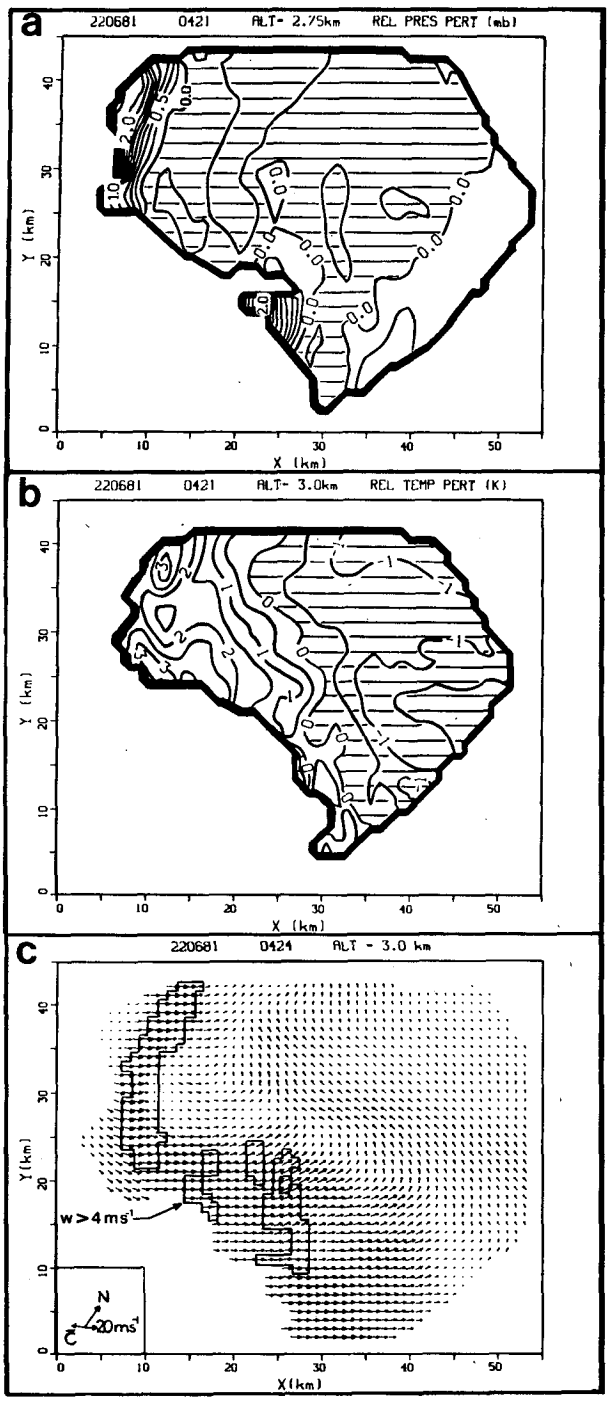

FIG. 9. As in Fig. 7 but for altitudes 2.75 and 3.0 km.

updraft (Fig. 3c). In these conditions hydrostatic pressure above 3000 m must be higher in the inflow region than in the inner region. Moreover, nonhydrostatic effects should be of less influence since the flow at these altitudes is rather uniformly a westerly one (Figs. 10c and 11c). As for the temperature field, it is less contrasted than at lower altitudes. It is worth noting that positive perturbations (up to 2°C with respect to the mean) interest a large area rearward, in correlation with the apparition of updrafts in the middle region ($15 < x < 20$ km). The fact that a negative temperature perturbation (with respect to the mean) is observed in the frontal updraft above 4000 m deserves some comment. Two effects acting

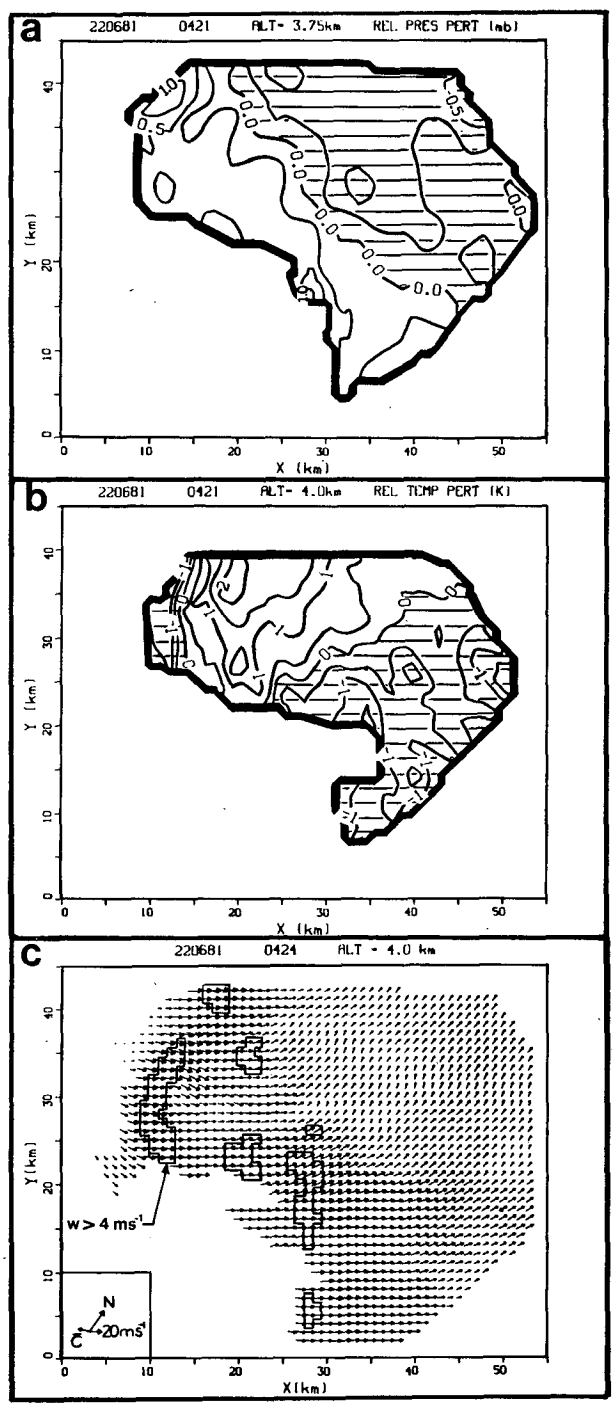

FIG. 10. As in Fig. 7 but for altitudes 3.75 and 4.0 km.

Unauthenticated | Downloaded 06/08/21 12:46 PM UTC

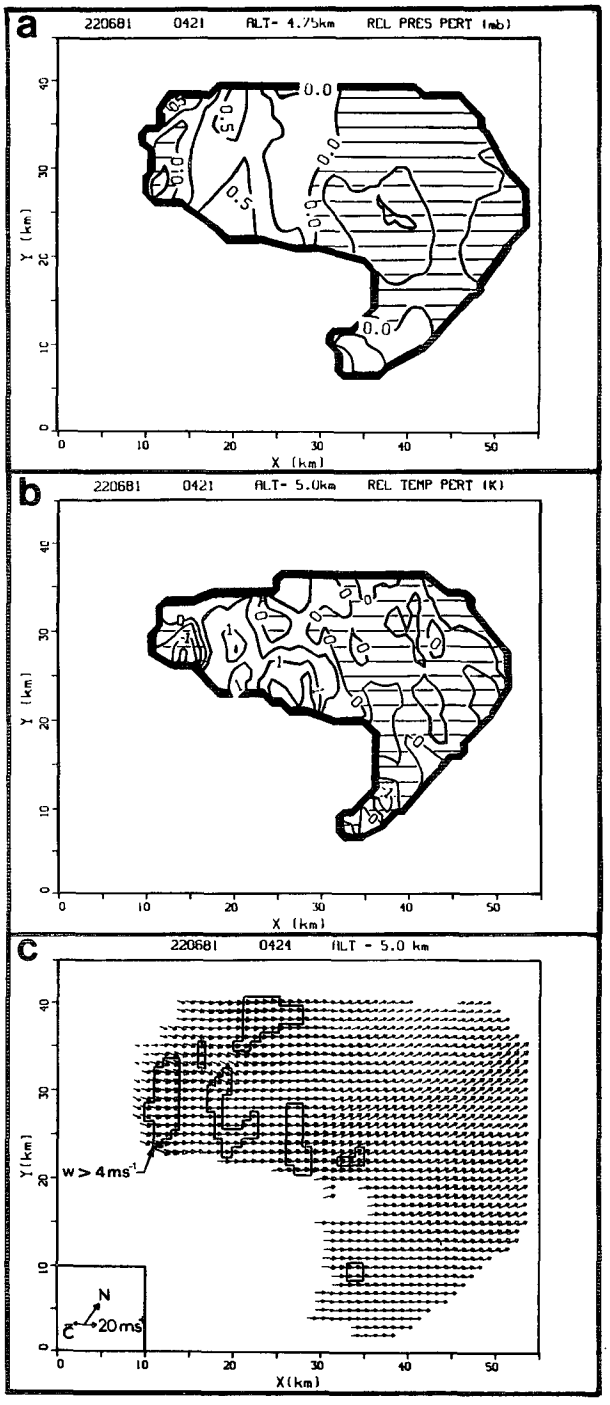

FIG. 11. As in Fig. 7 but for altitudes 4.75 and 5.0 km.

concurrently may explain the temperature deficit of the frontal updraft: First, the entrainment of environmental air (relatively cold at this height); second, the cloud water loading (it should be remembered that we measure the "virtual cloud temperature" perturbation defined as $\theta_{C1} = \theta_{V1} - q_c\theta_{V0}$), which may be quite important in the frontal updraft since the precipitation process has no time to release the condensed water. These two effects are certainly less effective in the updrafts of the middle region which are not subject to direct mixing with environmental air and in which a substantial part of the condensed water has been released to form the heavy precipitation core at front of the squall line.

In summary, the major points emerging from the present analysis are

- the potentially warm boundary layer air ahead the squall line is lifted up to about 2500 m by the frontward propagation of a cold air pool occupying the layer 0–2000 m.
- above 2500 m the frontal updraft becomes positively buoyant with respect to the environment, but the water loading and the entrainment of environmental air limit the ascent to 5000–6000 m.
- after release of the water loading by the precipitation process (producing the heavy precipitation core ahead the squall line), the air parcels recover a positive buoyancy and their ascent may start again (see Fig. 4c).
- between the main frontal updraft and the secondary one, an injection unperturbated air from about 3000 m may participate in the feeding of the cold air pool.

d. Discussion of the results

A conceptual model for the kinematic and thermodynamic processes occurring in the convective region of the 22 June 1981 squall line may be deduced from the present results (Fig. 12). It is to be outlined that these conclusions apply to be observations conducted within a limited region of the squall line and at one particular stage of its lifetime, so they are not necessarily valid for the whole mesoscale system (which extends over several hundreds kilometers) and at any stage of its lifetime.

The main characteristic of the circulation scheme proposed in Fig. 12 is the penetration of an intense frontward flow in the low levels of the convective region. This flow plays a prominent part in the dynamics since, below altitude 3000 m, it contributes to initiate and maintain the frontal updraft through the nonhydrostatic pressure perturbation (due to the collision between ambient air and propagation cold pool) and the temperature difference between entering air and colder frontward flow. Then the potentially unstable air is lifted up to the altitude of 3000 m from which thermally driven convection may develop. In the frontal updraft, mixing with the relatively cold air from the environment and cloud water loading reduces buoyancy, while in theinner region, once the water content is released through precipitations, weak convective updrafts appear. Although the local convective downdraft and direct inflow contribute

Unauthenticated | Downloaded 06/08/21 12:46 PM UTC

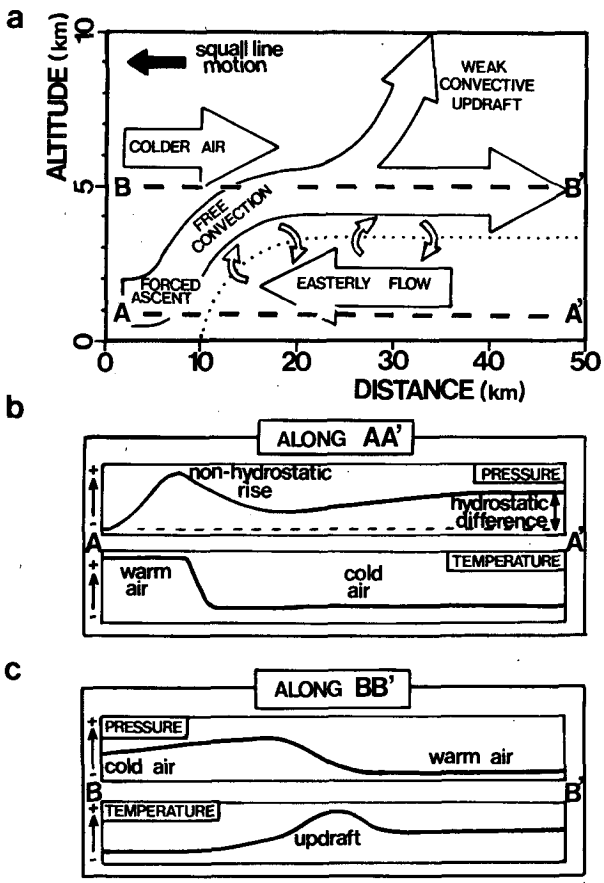

FIG. 12. (a) Conceptual model of the convective region of the 22 June 1981 squall line in the frame moving with the squall line. (b) Associated pressure and temperature perturbation profiles along *AA'*, at low levels. (c) Associated pressure and temperature perturbation profiles along *BB'*, at middle levels.

certainly to feed the low-level cold frontward flow, they are not intense enough to account completely for it. As deduced from wind profiles in the stratiform region (obtained from the VAD analysis of conical scans) the cold frontward flow results mainly from the propagation of a cold air pool produced by an evaporative mesoscale downdraft in the stratiform region (Chong, 1983).

These results present similarities with those obtained by Thorpe *et al.* (1982) with a two-dimensional model of a midlatitude squall line. In these simulations, the cumulonimbus were initiated by low-level convergence created by the propagation of a cold air pool spreading upstream at low levels, similar to the present low-level frontward flow. The two-dimensional wind field they obtain using the initial flow called [P(-5)] (Fig. 8a in Thorpe *et al.*, 1982) presents many similarities with the vertical cross section displayed here in Fig. 4c.

To our knowledge, the only comparable reconstruction of the thermodynamic structure of a tropical system of convective clouds was presented by LeMone (1983), hereafter referred to as LM. The data were from multi-aircraft passes at 8 levels from 150 to 5500 m above sea level through a squall line on 14 September 1974 observed during "GATE". The vertical cross sections (normal to the line's axis) of the composite mesoscale fields of horizontal and vertical wind velocities, pressure perturbation and equivalent potential temperature (Fig. 5 in LM) show similarities but also differences when compared with the present results.

Both observations display rather two-dimensional wind structures parallel to the squall-line displacement with air flowing through the front. The most intense updraft and the associated large reflectivity values are found in the frontal region near the leading edge of the cloud; behind the frontal region weaker vertical motions and precipitations contents are observed (Fig. 5a and 5b in LM, Fig. 4c here). Nevertheless some differences appear when comparing the role played by the convective downdraft and the low-level frontward flow in both cases. As seen in Fig. 5a and 5b in LM, a convective downdraft behind the frontal updraft induces below altitude 1000 m at the base of the updraft a density current and a gust front which contributes certainly to initiate the updraft. On the other hand, the frontward flow observed here extends up to the altitude 3000 m and forces the ascent of upstream air in the frontal updraft. The associated thermodynamic fields reflect these differences. The pressure and temperature perturbations are connected in LM (Fig. 5b and 5c) to the convective elements: temperature excess and pressure low are observed in the updraft, temperature deficit in the downdraft. The thermodynamic fields retrieved here at low-levels (Fig. 7, 8 and 9) reflect mainly the contrast between warm entering air and cold frontward flow. However, similarities in the pressure and temperature fields may also be outlined: the pressure high observed in Fig. 5c in LM below altitude 1000 m in connection with air from the convective downdraft could be in some degree similar to the positive pressure perturbation retrieved here at low levels (Figs. 7a, 8a and 9a) in front of the easterly flow. On the other hand, an association similar to that displayed in Fig. 5a and 5b in LM between updraft and positive temperature perturbation is observed here at altitude 3000 m for the frontal updraft (Fig. 9b) and above 3000 m for the weak convective updrafts in the inner convective region (Figs. 10b and 11b).

At least, another comparison deals with the propagation speed of both cloud systems. The convective band of 14 September 1974 (LM) moves very slowly (2, 5 m s^{-1}) whereas the propagation speed of the present squall line was rather fast (19 m s^{-1}). Following Charba (1974) and Wakimoto (1982), the density current model may be used to describe the motion of the gust front. The equation for the speed of the leading edge of a density current is

Unauthenticated | Downloaded 06/08/21 12:46 PM UTC

$$V = \mathrm{Fr}\left(gd\frac{\rho_c - \rho_w}{\rho_w}\right)^{1/2},$$

where g is the gravitational constant, ρ_c and d are the mean density and depth of the density current (here the frontward flow), ρ_w is the mean density of the ambient medium (here the upstream air), Fr the Froude number (ratio of the inertial force to the force of gravity). Using the values measured at ground level with the ALICE and DELTA stations and those retrieved up to altitude 3500 m from the radar data, yields for the 22 June 1981 squall line:

$$V = \mathrm{Fr} \times 22.30 \text{ m s}^{-1}.$$

Then the theoretical propagation speed V is equal to the observed one (19 m s^{-1}) if the Froude number Fr is taken equal to 0.85, which is not very different from the values obtained by Wakimoto (k = 0.77) or Charba (h = 1.08). Therefore the propagation of the cold air pool from the mesoscale downdraft in the stratiform region seems to play the major role in the dynamics of the 22 June 1981 squall-line.

A possible interpretation of the morphological differences between the line of cumulonimbus reported in LM and the 22 June 1981 squall line may lay in the fact that they were observed at different stages of their lifetime. As reported in Zipser *et al.* (1981) the cloud line, which has given rise to the convective band reported in LM, formed at about 1000 GMT while the aircraft observations extended from 1105 to 1526 GMT. Therefore this case study refers to a young or mature stage of the lifetime of the convective band, where the frontal convection is driven by thermal buoyancy. On the other hand the 22 June 1981 squall line was probably in a decaying stage at the time of observation, convective instability of inflowing air is weaker [as seen when comparing the thermodynamic structures of the upstream air in the present case (Fig. 2) and for the 14 September 1974 convective band (Fig. 13 in Zipser *et al.*, 1981)] and the frontal updraft is mainly forced by the propagation of the cold air pool from the evaporative downdraft in the stratiform region.

4. Conclusion

The combined use of dual-Doppler radar data and of the equation of motion has permitted the thermodynamic structure of a West-African squall line to be inferred, through horizontal fields of relative pressure and temperature perturbations. The present data fulfilled the requirements for such an analysis to be used, since both reflectivity and wind fields deduced from radar observations display stationary features and simple kinematic structures. Moreover "simultaneous" surface measurements provide an opportunity to test the results obtained from radar data at the lowest levels. Therefore the thermodynamic parameters retrieved from the radar data have been used to diagnose the dynamical processes involved in the observed airflow.

Although the present results seem encouraging, some ambiguities remain in our analysis due to the incomplete determination of the thermodynamic field, so that only *relative* pressure and temperature perturbations can be retrieved. As shown in Section 3, comparisons with surface network measurements may be helpful to remove this uncertainty, but this procedure can only be applied to low-level results. Likewise the combined use of instrumented aircraft measurements could provide supplementary information.

Nevertheless, the field description obtained from radar data is considerably larger than that deduced from *in situ* measurements. A promising possibility would be the simultaneous use of a simplified thermodynamic equation to determine the vertical temperature perturbation gradients so that the thermodynamic fields could be completely retrieved. However, such an analysis becomes essentially three-dimensional whereas the method used here refers to two-dimensional problems, so a suitable numerical method has to be defined.

Acknowledgments. The authors are indebted to Pr. R. Glowinski for suggesting the numerical method used to retrieve pressure and temperature fields. Financial and logistic support for the "COPT 81" experiment was provided by the Institut National d'Astronomie et de Géophysique, and the Direction des Recherches, Etudes et Techniques (France) and by the Ivorian Government. Thanks are due to Catherine Gal and Michelle Pennec for typing this manuscript.

APPENDIX A

Numerical Solving of the Variational Problems

1. Discretization

The functionals, to be minimized to retrieve pressure and temperature perturbations, may be written as

$$F = \iint_{D(z_0)} \left[\left(\frac{\partial C}{\partial x} - G_x\right)^2 + \left(\frac{\partial C}{\partial y} - G_y\right)^2\right] dxdy + \mu \iint_{D(z_0)} \left[\left(\frac{\partial^2 C}{\partial x^2}\right)^2 + 2\left(\frac{\partial^2 C}{\partial x \partial y}\right)^2 + \left(\frac{\partial^2 C}{\partial y^2}\right)^2\right] dxdy, \tag{A1}$$

where C denotes the values to be retrieved (pressure π_1 or "apparent" temperature θ_{C1} perturbations), $[G_x, G_y]$ the experimental estimates ($\mathbf{A}_H$ in (2) or $\mathbf{B}_H$ in (3)), $D(z_0)$ is the horizontal domain, at altitude z_0, where data $[G_x, G_y]$ is available.

Unauthenticated | Downloaded 06/08/21 12:46 PM UTC

As data $[G_x, G_y]$ is obtained at grid points, the first and second order derivatives of C are approximated numerically using a finite differences method. A single index K is used to denote the grid points as

$$K = (j - 1)N_x + i,$$

where i is varied from 1 to N_x along the X-axis and j from 1 to N_y along the Y-axis. Then (A1) may be discreterized as:

$$F = \sum_{K=1}^{N} [(\sum_{L=1}^{N} C_L \mathbf{M}^{KL} C_K) - 2\mathbf{W}^K C_K] + S, \quad \text{(A2)}$$

where $N = N_x \times N_y$. $\mathbf{M}^{KL}$ is a 17-banded matrix denoting connections between adjoining grid points, "vector" $\mathbf{W}^K$ includes the input data $[G_x, G_y]$, and S is a scalar. The minimization of F is achieved by the ensemble $[C_K; K = 1 \text{ to } N]$ which verifies:

$$\frac{\partial F}{\partial C_K} = 0 \quad \text{for} \quad K = 1 \text{ to } N. \quad \text{(A3)}$$

Since it derives from the quadratic positive definite form (A1), "matrix" $\mathbf{M}^{KL}$ is symmetric and positive definite. (A3) is then equivalent to

$$\sum_{L=1}^{N} [\mathbf{M}^{KL} C_L] = \mathbf{W}^K \quad \text{for} \quad K = 1 \text{ to } N, \quad \text{(A4)}$$

and it follows that

$$C_K = \sum_{L=1}^{N} [(\mathbf{M}^{KL})^{-1} W^L] \quad \text{for} \quad K = 1 \text{ to } N, \quad \text{(A5)}$$

where $(\mathbf{M}^{KL})^{-1}$ denotes the inverse matrix of $\mathbf{M}^{KL}$. The solution of (A5) is made easy by the simple structure of matrix $\mathbf{M}^{KL}$. For this reason the conjugate gradient algorithm (Polak, 1971) is an efficient method for the solution of this matrix equation.

2. Associated Euler equation and boundary conditions

For each point C_K, except on the boundary of the domain $D(z_0)$, (A4) is nothing else but a discretized form of the Euler equation for the minimization problem (A1), i.e.:

$$\left(\frac{\partial^2 C}{\partial x^2} + \frac{\partial^2 C}{\partial y^2}\right) - \mu\left(\frac{\partial^4 C}{\partial x^4} + 2\frac{\partial^4 C}{\partial x^2 \partial y^2} + \frac{\partial^4 C}{\partial y^4}\right) = \frac{\partial G_x}{\partial x} + \frac{\partial G_y}{\partial y}. \quad \text{(A6)}$$

Equation (A5) is then equivalent to the numerical integration of this Euler equation. The boundary conditions for this integration are provided through the truncated expressions of (A4) at the edges of $D(z_0)$. In the general case $\mu \neq 0$, it is shown that the truncated form of (A4) are discretized expressions of the following boundary conditions:

$$\left.\begin{aligned} &\frac{\partial C}{\partial n} - (\mu/\Delta)\frac{\partial^2 C}{\partial n^2} = G_n \\ &\frac{\partial^2 C}{\partial n^2} - (\mu/\Delta)(1 - \mu/\Delta^2)^{-1}\frac{\partial^3 C}{\partial n^3} = (1 - \mu/\Delta^2)^{-1}\frac{\partial G_n}{\partial n} \\ &\frac{\partial^3 C}{\partial n \partial s^2} = 0 \end{aligned}\right\}, \quad \text{(A7)}$$

where $\mathbf{n}$ and $\mathbf{s}$ are unit vectors respectively perpendicular and parallel to the boundary, s is the horizontal grid spacing (in the present case = 1000 m). The natural boundary conditions associated to the minimization problem (A1) (Courant and Hilbert, 1953) are

$$\left.\begin{aligned} &\frac{\partial C}{\partial n} - \mu\frac{\partial^3 C}{\partial n^3} = G_n \\ &\frac{\partial^2 C}{\partial n^2} = 0; \quad \frac{\partial^3 C}{\partial n \partial s^2} = 0 \end{aligned}\right\}. \quad \text{(A8)}$$

Equations (A7) and (A8) differ when μ becomes appreciable with respect to Δ^2. Nevertheless, the interest of using the "matrix" formulation (A4) result from the implicit taking into account of the boundary conditions so that nonrectangular boundaries or missing data do not create difficulties. When μ is equal to zero, (A7) and (A8) reduce to the natural boundary condition:

$$\frac{\partial C}{\partial n} = G_n.$$

APPENDIX B

Estimated Statistical Uncertainties

1. *A priori* estimates

Various sources of error can occur during the calculation of the input data [$\mathbf{A}_H$ in (2) and $\mathbf{B}_H$ in (3)] used to retrieve pressure and temperature perturbations: statistical error in radar data, estimate of the temporal derivatives $[\partial \mathbf{V}/\partial t]$ through differences between two successive scans, parameterization of the subgrid scale force, reflectivity–precipitating water content relationship. Among these, the only accessible contribution is that of statistical error in the cartesian components of velocity and their first order derivatives. In the present case, the calculated uncertainties in the three components of velocity (Testud and Chong, 1983; Chong and Testud, 1983) are

$$\left.\begin{aligned} \sigma^2(u) &\approx 0.25 \text{ m}^2 \text{ s}^{-2} \\ \sigma^2(v) &\approx 0.10 \text{ m}^2 \text{ s}^{-2} \\ \sigma^2(w) &\approx 0.95 \text{ m}^2 \text{ s}^{-2} \end{aligned}\right\}.$$

Unauthenticated | Downloaded 06/08/21 12:46 PM UTC

Any component of acceleration is calculated as

$$\frac{D\vartheta}{Dt} = \frac{\vartheta_2 - \vartheta_1}{\Delta t} + \frac{1}{2}\left[u_1\left(\frac{\partial\vartheta}{\partial x}\right)_1 + u_2\left(\frac{\partial\vartheta}{\partial x}\right)_2\right] + \frac{1}{2}\left[v_1\left(\frac{\partial\vartheta}{\partial y}\right)_1 + v_2\left(\frac{\partial\vartheta}{\partial y}\right)_2\right] + \frac{1}{2}\left[w_1\left(\frac{\partial\vartheta}{\partial z}\right)_1 + w_2\left(\frac{\partial\vartheta}{\partial z}\right)_2\right],$$

where ϑ stands for u, v or w, subscript 1 and 2 refer to each of two successive scans and t is the time lag between scans 1 and 2. Then, when supposing that errors are identical for both scans, the contribution of radar *statistical* error in the calculated accelerations may be estimated through

$$\sigma^2\left(\frac{Du}{Dt}\right) \sim \left\{2\frac{[1 - C(\Delta_H)]}{\Delta_H^2}(\langle u^2\rangle + \langle v^2\rangle) + \frac{2}{\Delta_z^2}\langle w^2\rangle + \left\langle\left(\frac{\partial u}{\partial x}\right)^2\right\rangle\right\}\sigma^2(u) + \left\langle\left(\frac{\partial u}{\partial y}\right)^2\right\rangle\sigma^2(v) + \left\langle\left(\frac{\partial u}{\partial z}\right)^2\right\rangle\sigma^2(w), \quad \text{(B1)}$$

$$\sigma^2\left(\frac{Dv}{Dt}\right) \sim \left\{2\frac{[1 - C(\Delta_H)]}{\Delta_H^2}(\langle u^2\rangle + \langle v^2\rangle) + \frac{2}{\Delta_z^2}\langle w^2\rangle + \left\langle\left(\frac{\partial v}{\partial y}\right)^2\right\rangle\right\}\sigma^2(v) + \left\langle\left(\frac{\partial v}{\partial x}\right)^2\right\rangle\sigma^2(u) + \left\langle\left(\frac{\partial v}{\partial z}\right)^2\right\rangle\sigma^2(w), \quad \text{(B2)}$$

$$\sigma^2\left(\frac{Dw}{Dt}\right) \sim \left\{\frac{2}{\Delta_H^2}(\langle u^2\rangle + \langle v^2\rangle) + \frac{2}{\Delta_z^2}\langle w^2\rangle + \left\langle\left(\frac{\partial w}{\partial z}\right)^2\right\rangle\right\}\sigma^2(w) + \left\langle\left(\frac{\partial w}{\partial x}\right)^2\right\rangle\sigma^2(u) + \left\langle\left(\frac{\partial w}{\partial y}\right)^2\right\rangle\sigma^2(v), \quad \text{(B3)}$$

where $C(\Delta_H)$ is the autocorrelation function expressing the noise reduction due to filtering (Testud and Chong, 1983), Δ_H and Δ_z are respectively the horizontal and vertical grid spacing (in the present case $\Delta_H = 1000$ m, $\Delta_z = 500$ m).

Then, *statistical uncertainty* in the input values $\mathbf{A}_H$ in (2) may be simply deduced from (B1) and (B2), for each horizontal plane, through

$$\sigma^2(\mathbf{A}_H) = \sigma^2(A_x) + \sigma^2(A_y) \sim [C_p\theta_{V0}]^{-2}[\sigma^2(Du/Dt) + \sigma^2(Dv/Dt)]. \quad \text{(B4)}$$

Likewise, when supposing that error in the retrieved horizontal pressure perturbation gradients is reduced by a factor 2.2 with respect to that in the input values $\mathbf{A}_H$ (see section 2 below), *statistical uncertainty* in the input values $\mathbf{B}_H$ in (3) may be estimated from (B3) and (B4), for each horizontal plane, through

$$\sigma^2(\mathbf{B}_H) = \sigma^2(B_x) + \sigma^2(B_y) \sim [C_p\theta_{V0}^2/g]^2\left[\frac{0.4}{\Delta_z^2}\sigma^2(\mathbf{A}_H)\right] + [\theta_{V0}/g]^2\left[\frac{2}{\Delta_H^2}\sigma^2(Dw/Dt)\right]. \quad \text{(B5)}$$

2. *A posteriori* estimates

Following Gal-Chen and Hane (1981) the reliability of the retrieved pressure and temperature fields may be quantified through the standard deviation between the input data and the retrieved gradients. Using notations of Appendix A, the quantity E_R is defined by

$$E_R = \frac{\iint_{D(z_0)}\left[\left(\frac{\partial C}{\partial x} - G_x\right)^2 + \left(\frac{\partial C}{\partial y} - G_y\right)^2\right]dxdy}{\iint_{D(z_0)}[G_x^2 + G_y^2]dxdy},$$

where $[G_x, G_y]$ are the input data [$\mathbf{A}_H$ in (2) or $\mathbf{B}_H$ in (3)], C denotes the values to be retrieved (pressure π_1 or "apparent" temperature θ_{C1} perturbations) and $D(z_0)$ is the horizontal domain, at altitude z_0, where data is available.

Relevance of parameter E_R has been evaluated through numerical tests with simulated data. Let us first outline that these tests have been restricted to the "mathematical" influence of a *random statistical error.* On the other hand, the only way for estimating the influence of a *systematic error* is to compare the results obtained with independent measurements of pressure or temperature (see Section 3b). As a matter of fact, this last kind of error may induce inextricable biases in the input data in such a way that the obtained results could be mathematically satisfying but physically inconsistent.

In these conditions, the conclusions that can be drawn from numerical tests conducted with simulated data with characteristic wavelengths larger than 3.7 s (since smaller wavelengths have been filtered out in the processing of radar data) are the following:

1. if the input data [$\mathbf{G}_H$] are exact gradients [$\nabla_H C_0$] (no noise is added), the numerical integration of the Euler equation (through (A5) in Appendix A) leads to small errors in the output gradients $\nabla_H C^*$, depending on the characteristic wavelength of the input data. E_R (which is identical to a relative error in this case) is smaller than 0.01 for wavelengths larger than $10\Delta_H$, and is, for example, equal to 0.05 for a wavelength equal to $5\Delta_H$.

2. if the input data are exact gradients plus independent random (gaussian white) noise ϵ_H, two un-

Unauthenticated | Downloaded 06/08/21 12:46 PM UTC

equivocal relationships are found, whatever the wavelength of the exact gradients and the rms value of noise $[\langle \epsilon_H^2 \rangle^{1/2}]$ are

i) between E_R and the relative error σ_{in}^2 in the input data:

$$\sigma_{\text{in}}^2 \sim 1.6 E_R \tag{B6}$$

with

$$\sigma_{\text{in}}^2 = \frac{\iint_{D(z_0)} [\epsilon_H^2] dxdy}{\iint_{D(z_0)} [\mathbf{G}_H^2] dxdy}.$$

ii) between σ_{in}^2 and the relative standard deviation σ_{out}^2 between the retrieved gradients $\nabla_H C^*$ and the exact ones $\nabla_H C_0$:

$$\sigma_{\text{out}}^2 \sim 0.2 \sigma_{\text{in}}^2 \tag{B7}$$

with

$$\sigma_{\text{out}}^2 = \frac{\iint_{D(z_0)} [\nabla_H C^* - \nabla_H C_0]^2 dxdy}{\iint_{D(z_0)} [\mathbf{G}_H^2] dxdy}.$$

Equation (B7) implies that statistical error is reduced by a factor 2.2 ($=\sigma_{\text{in}}/\sigma_{\text{out}}$). The "input noise vector" ϵ_H, as any two-dimensional vector, may be expressed as

$$\epsilon_H = \nabla_H Q + (\nabla \times \mathbf{R})_H,$$

where Q is a scalar field and $\mathbf{R}$ a three-dimensional vector field. Then, minimization of functional F_1 in (5) (Section 2b) allows only the "divergence-free" part $(\nabla \times \mathbf{R})_H$ of ϵ_H to be filtered out (since its "curl-free" part, $\nabla_H Q$ is indistinguishable from the actual gradients), and this leads to a reduction in statistical error by a factor 2. Moreover, the combined minimization of constraint F_2 in (5) allows to eliminate the contribution of random error (both "curl and divergence-free" parts) for wavelengths smaller than $3.7\Delta_H$ and increases the error reduction factor.

3. if the input data are independent random (gaussian white) noises, E_R is equal to its maximum value 0.60. Likewise the small wavelengths are cancelled out through constraint, while for larger wavelengths only the "divergence-free" part can be filtered.

Therefore, at each altitude z_0, the value of E_R (for both pressure and temperature fields) indicates the reliability of the retrieved results since E_R is proportional to both input and output relative *statistical* errors. Moreover estimates of these relative errors may be obtained from E_R through (B6) and (B7) and compared to the *a priori* estimates of statistical uncertainties (due to radar error) in the input data $\mathbf{A}_H$ and $\mathbf{B}_H$ calculated with (B4) and (B5).

REFERENCES

Charba, J., 1974: Application of gravity current model to analysis of squall line gust front. *Mon. Wea. Rev.*, **104**, 140–156.

Chong, M., 1983: Les radars météorologiques Doppler pour l'étude de la convection orageuse: Application à l'étude d'une ligne de grains tropicale. Thèse de Doctorat d'Etat, Université de Paris VI, 140 pp.

——, and J. Testud, 1983: Three-dimensional wind field analysis from dual-Doppler radar data. Part III. The boundary condition: An optimum determination based on a variational concept. *J. Climate Appl. Meteor.*, **22**, 1227–1241.

——, F. Roux and J. Testud, 1980: A new filtering and interpolating method for processing dual-Doppler radar data: Performance in three-dimensional wind restitution, ability to derive pressure and temperature fields. *Preprints, 19th Conf. Radar Meteorology*, Miami Beach, Amer. Meteor. Soc., 286–293.

——, J. Testud and F. Roux, 1983: Three-dimensional wind field analysis from dual-Doppler radar data. Part II: Minimizing the error due to temporal evolution. *J. Climate Appl. Meteor.*, **22**, 1216–1226.

Cotton, W. R., and G. L. Tripoli, 1978: Cumulus convection in shear flow: Three-dimensional numerical experiments. *J. Atmos. Sci.*, **35**, 1503–1521.

Courant, R., and D. Hilbert, 1953: *Methods of Mathematical Physics, Vol. 1*, (Chap. 4), Interscience, 561 pp.

Deardorff, J. W., 1975: The development of boundary layer turbulence models for use in studying the severe storm environment. *Proc. SESAME Open Meeting*, D. K. Lilly, Ed., Boulder, NOAA Environ. Res. Laboratories, 251–264.

Gal-Chen, T., 1978: A method for initialization of the anelastic equations: implications for matching models with observations. *Mon. Wea. Rev.*, **106**, 587–606.

——, and C. E. Hane, 1981: Retrieving buoyancy and pressure fluctuations from Doppler radar observations: A status report. Progress in radar technology. *Atmos. Technol.*, **13**, 98–104.

——, and R. A. Kropfli, 1983: Deduction of thermodynamic properties from dual-Doppler radar observations in the PBL. *Preprints, 21st Conf. Radar Meteorology*, Edmonton, Amer. Meteor. Soc., 33–38.

Hane, C. E., and B. C. Scott, 1978: Temperature and pressure perturbations within convective clouds derived from detailed air motions: Preliminary testings. *Mon. Wea. Rev.*, **106**, 654–661.

——, and T. Gal-Chen, 1982: Derivation of thermodynamic variables in thunderstorms and in the boundary layer. *Preprints 12th Conf. Severe Local Storms*, San Antonio, Amer. Meteor. Soc., 520–523.

——, R. B. Wilhelmson and T. Gal-Chen, 1981: Retrieval of thermodynamic variables within deep convective clouds: Experiments in three dimensions. *Mon. Wea. Rev.*, **109**, 564–576.

Heymsfield, G. M., 1978: Kinematic and dynamic aspects of the Harrah tornadic storm analyzed from dual-Doppler radar data. *Mon. Wea. Rev.*, **106**, 233–254.

Houze, R. A., and A. K. Betts, 1981: Convection in GATE. *Rev. Geophys. Space Phys.*, **19**, 541–576.

Johnson, R. H., and M. E. Nicholls, 1983: A composite analysis of the boundary layer accompanying a tropical squall-line. *Mon. Wea. Rev.*, **111**, 308–319.

Klemp, J. B., and R. B. Wilhelmson, 1978: The simulation of three-dimensional convective storm dynamics. *J. Atmos. Sci.*, **35**, 1070–1096.

——, —— and P. S. Ray, 1981: Observed and numerically simulated structure of a mature supercell thunderstorm. *J. Atmos. Sci.*, **38**, 1558–1580.

Kropfli, R. A., and L. J. Miller, 1976: Kinematic structure and

Unauthenticated | Downloaded 06/08/21 12:46 PM UTC

flux quantities in a convective storm from dual-Doppler radar observation. *J. Atmos. Sci.*, **33**, 520–529.

Le Mone, M. A., 1983: Momentum transport by a line of cumulonimbus. *J. Atmos. Sci.*, **40**, 1815–1834.

Lhermitte, R., 1970: Doppler radar methodology for the observation of convective storms. *Preprints, 14th Conf. Radar Meteorology*, Boston, Amer. Meteor. Soc., 133–138.

Pasken, R., and Y. J. Lin, 1982: Pressure perturbations within a tornadic storm derived from dual-Doppler wind data. *Preprints, 12th Conf. Severe Local Storms*, San Antonio, Amer. Meteor. Soc., 257–260.

Polak, E., 1971: Computational methods and optimization: A unified approach. *Math. Sci. Eng.*, **77**, 312 pp.

Ray, P. S., R. J. Doviak, G. B. Walker, D. Sirmans, J. Carter and B. Bumgarner, 1975: Dual-Doppler observation of a tornadic storm. *J. Appl. Meteor.*, **14**, 1521–1530.

Roux, F., and J. Testud, 1983: Pressure and temperature fields retrieved from dual-Doppler radar observation of a West-African squall line. *Preprints, 21st Conf. Radar Meteorology*, Edmonton, Alta., Amer. Meteor. Soc., 27–32.

——, ——, B. Pinty and J. P. Chalon, 1982: Dual-Doppler radar and surface network observations of a West-African squall line during the "COPT 81" experiment. *Preprints, Conf. Cloud Physics*, Chicago, Amer. Meteor. Soc., 547–550.

Schlesinger, R. E., 1978: A three-dimensional numerical model of an isolated thunderstorm. Part I: Comparative experiments for variable ambient shear. *J. Atmos. Sci.*, **35**, 690–713.

Smagorinsky, J., 1963: General circulation experiments with the primitive equations. I: The basic experiments. *Mon. Wea. Rev.*, **91**, 99–164.

Sommeria, G., and J. Testud, 1984: "COPT 81", a field experiment designed for the study of deep convection in continental tropical regions. *Bull. Amer. Meteor. Soc.* **65**, 4–10.

Testud, J., and M. Chong, 1983: Three-dimensional wind field analysis from dual-Doppler radar data. Part I: Filtering, interpolating and differentiating the raw data. *J. Climate Appl. Meteor.*, **22**, 1204–1215.

Thorpe, A. J., M. J. Miller and M. W. Moncrieff, 1982: Two-dimensional convection in non-constant shear: A model of mid-latitude squall lines. *Quart. J. Roy. Meteor. Soc.*, **108**, 739–762.

Wahba, G., and J. Wendelberger, 1980: Some new mathematical methods for variational objective analysis using splines and cross validation. *Mon. Wea. Rev.*, **108**, 1122–1143.

Wakimoto, R. M., 1982: The life cycle of thunderstorm gust fronts as viewed with Doppler radar and rawinsonde data. *Mon. Wea. Rev.*, **110**, 1060–1082.

Wilhelmson, R. B., 1974: The life cycle of a thunderstorm in three dimensions. *J. Atmos. Sci.*, **31**, 1629–1651.

Zipser, E. J., 1977: Mesoscale and convective-scale downdrafts as distinct components of squall line circulation. *Mon. Wea. Rev.*, **110**, 1568–1589.

——, R. J. Meitin and M. A. Lemone, 1981: Mesoscale motion fields associated with a slowly moving GATE convective band. *J. Atmos. Sci.*, **38**, 1725–1750.

Unauthenticated | Downloaded 06/08/21 12:46 PM UTC